# Accuracy of Estimates of Cardiac Action Potential Duration from Extracellular Waveforms Simulated by the Bidomain Model

P Colli Franzone[1], LF Pavarino[2], S Scacchi[2], B Taccardi[3]

[1]Department of Mathematics, University of Pavia, Italy
[2]Department of Mathematics, University of Milan, Italy
[3]CVRTI, University of Utah, USA

## Abstract

*The goal of the present work is to provide an extensive quantitative analysis of the accuracy of activation - recovery intervals (ARIs) derived from unipolar electrograms (EGs) and hybrid monophasic action potentials (HMAPs) under normal and ischemic conditions. ARIs are compared with the gold standard action potential durations (APDs) based on the transmembrane action potential (TAP). This study is based on large scale parallel 3D numerical simulations of the action potential propagation modeled by the anisotropic Bidomain system coupled with the Luo-Rudy I membrane model. The results show a very good overall accuracy of ARI estimates of APD, with quite low mean discrepancies and standard deviations. The correlation coefficients between ARI and APDs are not as good as the ones of the associated repolarization time (RT) markers, but are always greater than 0.90 except for some homogeneous and ischemic slabs. While highly reliable repolarization sequences can be derived from extracellular RT markers, ARI spatial distributions are not always locally accurate and well correlated estimates of the associated APD spatial distributions. In particular, EG-based ARIs can fail near the borders of the ischemic region (e.g. in presence of linear ST ramp or in absence of a T wave), and in such cases HMAP-based ARIs may offer reliable alternatives for estimating APDs.*

## 1. Introduction

Activation - recovery intervals (ARIs) and action potential durations (APDs) play an important role in the study of the mechanisms underlying the genesis of cardiac arrhythmias. While activation times (ATs) are easily determined, there are still uncertainties about the best method for determining repolarization times (RTs) and ARI from extracellular recordings. In our previous study [1], we performed a quantitative analysis of the accuracy of repolarization time (RT) markers derived from unipolar electrograms (EGs) and hybrid monophasic action potentials (HMAPs). These markers have been compared with the gold standard RT markers derived from transmembrane action potentials (TAPs), i.e. the instant $RT_{tap}$ of minimum downslope (fastest repolarization) and the instant $RT90_{tap}$ when the TAP reaches the 90% of the resting value (late repolarization phase), both during downstroke.

The most widely used EG-based RT marker is the instant $RT_{eg}$ of occurrence of the maximum time derivative during the T wave [2, 3]. We have also proposed in [4] the marker for late repolarization $RT90_{eg}$, defined by the minimum second time derivative of the EG waveform during the T wave. Alternative extracellular RT markers are based on bipolar signals recorded taken the difference between the EG at a fixed site inside an area permanently depolarized (PD), created e.g. by pressure, suction or KCl injection, and the EGs of exploring sites. When the exploring and PD sites are very close to each other, we obtain the so-called monophasic action potential (MAP), see e.g. [5], while when considering a generic exploring site, we obtain the so-called hybrid monophasic action potentials (HMAP), see e.g. [6]. While TAP and MAP techniques can not be performed extensively in in vivo measurements, EG and HMAP recording can be applied in large regions of a beating heart in in vivo studies to map excitation and repolarization sequences. Since the HMAP waveforms exhibit a monophasic downstroke phase, they contain valuable information about the repolarization time of the exploring site, see [7]. Hence, the HMAP-based markers $RT_{hmap}$ and $RT90_{hmap}$ are defined in the same way as the TAP repolarization markers.

This paper extends our previous quantitative analysis of RT markers to the accuracy of ARI and APD spatial distributions. In particular, we will assess the performance of $ARI_{eg} = RT_{eg} - AT_{eg}$, $ARI_{hmap} = RT_{hmap} - AT_{hmap}$ as estimates of APD and of $ARI90_{eg} = RT90_{eg} - AT_{eg}$, $ARI90_{hmap} = RT90_{hmap} - AT_{hmap}$ as estimates of APD90.

## 2. Methods

**The Bidomain model**. We base our simulations on the Bidomain model (see [8]), describing the intra and extracellular potentials $u_i(\mathbf{x},t), u_e(\mathbf{x},t)$, gating variables $w(\mathbf{x},t)$ and ionic concentrations $c(\mathbf{x},t)$, as solutions of the reaction-diffusion system

$$\begin{cases} c_m \dfrac{\partial v}{\partial t} - \mathrm{div}(D_i \nabla u_i) + i_{ion}(v,w,c) = -i_{app} \\ -c_m \dfrac{\partial v}{\partial t} - \mathrm{div}(D_e \nabla u_e) - i_{ion}(v,w,c) = i_{app} \\ \dfrac{\partial w}{\partial t} - R(v,w) = 0, \qquad \dfrac{\partial c}{\partial t} - S(v,w,c) = 0 \\ \mathbf{n}^T D_{i,e} \nabla u_{i,e} = 0 \\ v(\mathbf{x},0) = v_0(\mathbf{x}),\ w(\mathbf{x},0) = w_0(\mathbf{x}),\ c(\mathbf{x},0) = c_0(\mathbf{x}). \end{cases}$$

Here $v(\mathbf{x},t) = u_i(\mathbf{x},t) - u_e(\mathbf{x},t)$ is the transmembrane potential, $c_m$, $i_{ion}$, $i_{app}$ the capacitance , the ionic current of the membrane and the applied intra- and extra-cellular currents per unit volume, respectively. $i_{ion}$, $R$ and $S$ are here given by the Luo-Rudy I model (LR1, [9]). $D_{i,e}$ are the anisotropic conductivity tensors built from a fiber structure with $90^o$ rotation from endo to epicardium and laminar structure, yielding an orthotropic anisotropy of the cardiac tissue, see [10] for details. We discretize this system by trilinear finite elements in space and semi-implicit finite differences in time [11]. The parallel code is based on the PETSc parallel library [12] and is run on a Linux cluster.

**Multi-electrode array and electrograms.** The cardiac domain $H$ considered in this study is a cartesian slab of dimensions $1.92 \times 1.92 \times 0.48\ cm^3$, modeling a portion of the left ventricular wall. In this slab, we consider a matrix of 12×12 exploring multielectrode needles spaced 1.6 $mm$ from each other and 0.8 $mm$ from the slab boundary, as shown in Fig. 1. Each needle carries 13 recording sites, spaced 0.4 $mm$ along the shank. We then have 12×12 sites on each of the 13 intramural planes, for a total of 12×12×13 = 1872 recording sites in the slab, each recording the intra and extracellular potentials.

**Permanently depolarized (PD) volume.** A permanently depolarized (PD) site is obtained by assigning the extracellular potassium concentration equal to the intracellular one, i.e. $I_{K1}$ is zero in the small PD volume. We considered different locations for the PD site, see Fig. 1, all with dimensions $0.8 \times 0.8 \times 0.8\ mm^3$. Given a point $\mathbf{x}_{PD}$ in the PD volume, the HMAP at a generic point $\mathbf{x}$ in the domain is given by $hmap(\mathbf{x},t) = u_e(\mathbf{x}_{PD},t) - u_e(\mathbf{x},t)$.

**Subendocardial ischemia.** We consider five different types of slabs, one with homogeneous (H-slab) and two with heterogeneous (3-slab, W-slab) intrinsic cellular properties, one with a subendocardial moderate ischemic region (MI-slab) and one with a severe ischemic region (SI-slab). The ischemic region has dimensions $0.4 \times 0.4 \times 0.16\ \ cm^3$ and is located at the center of the slab as shown in Fig. 1. In the LR1 model, the current $I_K$ is scaled by a factor 2.325. Inside the ischemic region, the extracellular potassium concentration $[K]_o$ is increased from $5.4\,mM$ (control) to $10.5\,mM$ (MI-slab) and $18\,mM$ (SI-slab), yielding resting potential and APD90 of $-84\,mV$ and $250\,ms$ (control), $-70\,mV$ and $150\,ms$ (MI-slab), $-55\,mV$ and $60\,ms$ (MI-slab); see [10, 13, 14] for details of the parameters calibration.

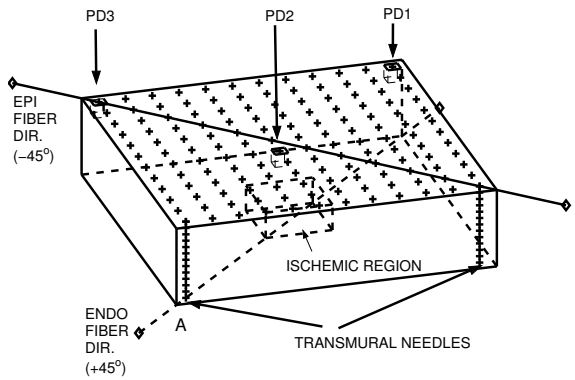


Figure 1. Cardiac slab $H$, Permanently Depolarized (PD) sites, subendocardial ischemic region, transmural needles.

**Stimulation site.** Intra- and extra-cellular stimuli are applied ($i_{app} = -250\ mA/cm^3$ for 1 ms) in a small volume (3 mesh points in each direction) at site $A$ in Fig. 1.

**Postprocessing**. The extra- and intracellular potential waveforms $u_e(x,t)$ and $u_i(x,t)$ are stored at the $12 \times 12 \times 13$ locations of the multi-electrode array. The reference potential is here chosen as the average extracellular potential over the cardiac volume $H$. From the $u_e$ and $v = u_i - u_e$ waveforms, we then compute the RT and ARI markers previously defined. The TAP markers and APD are assumed to be the gold standard in our reliability analysis.

## 3. Results

For each of the five slab types (H-slab, 3-slab, W-slab, MI-slab, SI-slab), we simulate the excitation and repolarization processes elicited by a local stimulus applied at the location $A$ in Fig. 1. HMAPs are computed using the PD3 location. We evaluate the ARIs overall performance of the EG and HMAP markers for the five simulations, disregarding RT marker values related to sites within the inexcitable regions, i.e. the PD volume and the ischemic region in the SI case.

Table 1 reports the comparison between the ARI estimates ($\mathrm{ARI}_{eg}$ vs APD, $\mathrm{ARI}_{hmap}$ vs APD, $\mathrm{ARI90}_{eg}$ vs APD90, $\mathrm{ARI90}_{hmap}$ vs APD90). The results show that all ARI estimates provide very reliable estimates of

| | ARI$_{eg}$ v APD | | | ARI$_{hmap}$ v APD | | |
|---|---|---|---|---|---|---|
| | mean | std | corr | mean | std | corr |
| **H-slab** | 2.14 | 1.98 | 0.84 | 1.83 | 1.60 | 0.77 |
| **3-slab** | 1.92 | 1.65 | 0.95 | 2.39 | 2.23 | 0.94 |
| **W-slab** | 1.39 | 1.19 | 0.96 | 2.09 | 2.18 | 0.92 |
| **MI-slab** | 2.16 | 2.23 | 0.91 | 1.94 | 2.22 | 0.93 |
| **SI-slab** | 2.01 | 1.67 | 0.90 | 1.90 | 1.80 | 0.84 |
| | ARI90$_{eg}$ v APD90 | | | ARI90$_{hmap}$ v APD90 | | |
| | mean | std | corr | mean | std | corr |
| **H-slab** | 0.95 | 0.86 | 0.91 | 3.04 | 2.15 | 0.72 |
| **3-slab** | 1.63 | 1.75 | 0.94 | 5.26 | 2.45 | 0.92 |
| **W-slab** | 1.04 | 1.09 | 0.98 | 5.10 | 1.99 | 0.95 |
| **MI-slab** | 1.31 | 1.91 | 0.95 | 3.07 | 2.24 | 0.90 |
| **SI-slab** | 1.34 | 2.19 | 0.90 | 2.95 | 2.13 | 0.63 |

Table 1. ARI and APD discrepancies. mean = average absolute difference (over all 1872 recording sites); std = standard deviation; corr = correlation coefficient.

| | APD | ARI$_{eg}$ | ARI$_{hmap}$ |
|---|---|---|---|
| **H-slab** | 2.83 | 5.26 | 5.49 |
| **3-slab** | 20.37 | 17.11 | 16.10 |
| **W-slab** | 17.79 | 15.23 | 14.18 |
| | APD90 | ARI90$_{eg}$ | ARI90$_{hmap}$ |
| **H-slab** | 3.20 | 3.97 | 5.22 |
| **3-slab** | 19.68 | 16.87 | 17.94 |
| **W-slab** | 17.32 | 14.66 | 13.98 |

Table 2. ARI and APD average transmural dispersions (over the $12 \times 12 = 144$ recording needles).

the reference APD. In terms of accuracy, ARI90$_{eg}$ exhibits the best performance, with mean discrepancy (mean) |ARI90$_{eg}$ - APD90| bounded by 1.63 and standard deviation (std) bounded by 2.19. ARI$_{eg}$ and ARI$_{hmap}$, as estimates of APD, show comparable overall performance, with mean discrepancies |ARI$_{eg}$ - APD| and |ARI$_{hmap}$ - APD| bounded by 2.16 $ms$ and 2.39 $ms$, respectively, and std bounded by 2.23. ARI90$_{hmap}$ exhibits larger discrepancies for each slab type, reaching mean 5.26 $ms$ and std 2.45 for the 3-slab. The correlation coefficients (corr) between EG-based ARI and APD markers are always greater than 0.90 except for H-slab (0.84). The same holds for the correlation coefficients of HMAP-based ARI and APD markers, except for H-slab and SI-slab, where they decrease to 0.63.

Table 2 reports the ARI and APD average transmural dispersions over the $12 \times 12 = 144$ recording needles. All ARIs distinguish the different types of transmural heterogeneity, but in general underestimate the transmural APD dispersion in heterogeneous 3-slab and W-slab, while they overestimate it in H-slab. Fig. 2 shows some examples of transmural RT profiles (left) and ARI, APD profiles (right)

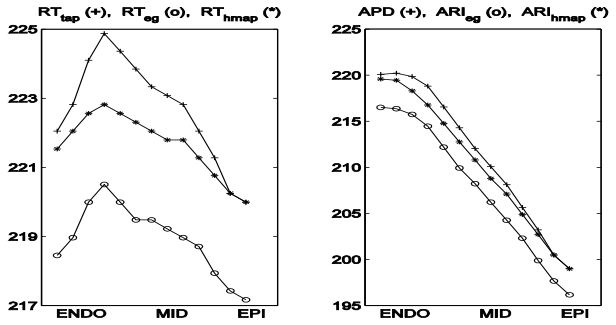


Figure 2. Transmural profiles of RT$_{tap}$ (+), RT$_{eg}$ (o), RT$_{hmap}$ (*) (left), and of APD (+), ARI (o), ARI$_{hmap}$ (*) (right) for needle (1,1) of W-slab.

along needle (1,1) of W-slab. RT$_{eg}$ and RT$_{hmap}$ underestimate and shift downward the reference RT$_{tap}$ profile, so the same happens for the ARI$_{eg}$ and ARI$_{hmap}$ profiles with respect to the reference APD profile (the RT - RT$_{tap}$ discrepancies in the left plot and ARI - APD discrepancies in the right plot are essentially the same but the scales of the two plots are different). The qualitative behavior of ARI$_{eg}$ and ARI$_{hmap}$ matches well the reference APD profile.

In spite of the good overall accuracy of ARI estimates of APDs, local inaccuracies might still be present. Fig. 3 shows the ARI and APD maps reconstructed from the multielectrode array on a transmural diagonal plane of W-slab. Indeed, discrepancies are present in the ARI$_{eg}$ map (middle, corr$_1$ = 0.83) and even worse in the ARI$_{hmap}$ map (bottom, corr$_2$ = 0.43). The situation improves considerably by considering late repolarization markers, as illustrated by Fig. 4 showing smaller discrepancies in the ARI90$_{eg}$ map (middle, corr$_1$ = 0.96) and in the ARI90$_{hmap}$ map (bottom, corr$_2$ = 0.92). Analogous local discrepancies are present in both ischemic MI- and SI-slabs (not shown), in particular near the critical intramural region above the ischemic region.

## 4. Conclusion

The results of our 3D Bidomain simulation study show a very good overall accuracy of ARI$_{eg}$, ARI$_{hmap}$ as estimates of APD and of ARI90$_{eg}$, ARI90$_{hmap}$ as estimates of APD90, showing in all cases quite low mean discrepancies and standard deviations. The correlation coefficients between ARI and APDs are not as good as the ones of the associated repolarization time (RT) markers (this is indeed possible since the correlation function is not linear in its arguments), but are always greater than 0.90 except for some homogeneous and ischemic slabs. While highly reliable repolarization sequences can be derived from extracellular RT markers, ARI spatial distributions are not always locally accurate and well correlated estimates of

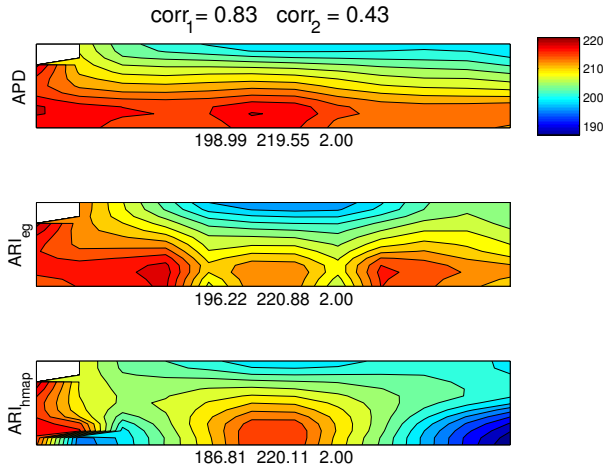


Figure 3. ARI and APD maps reconstructed from multielectrode array on transmural diagonal plane of W-slab. Below each panel are the maximum, minimum and step in ms of the displayed map; PD site is in top-left corner.

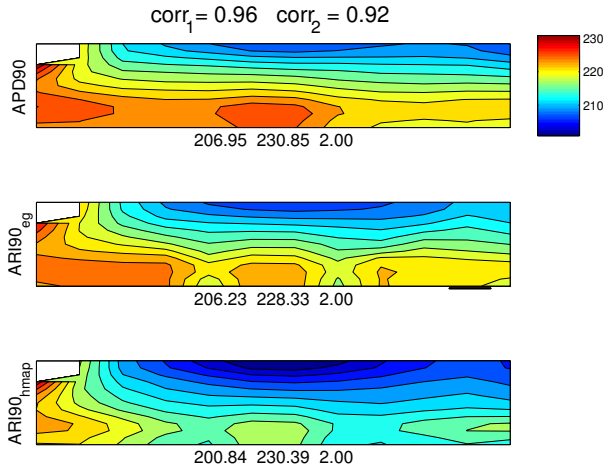


Figure 4. ARI90 and APD90 maps reconstructed from multielectrode array on transmural diagonal plane of W-slab. Same format as Fig. 3.

the associated APD spatial distributions. ARI transmural profiles correctly detect the size of the ischemic regions, except for the sizes detected by $ARI_{eg}$, which are generally overestimated. In particular, EG-based ARIs can fail near the borders of the ischemic region (e.g. in presence of linear ST ramp or in absence of a T wave), and in such cases HMAP-based ARIs may offer reliable alternatives for estimating APDs.

## References


[1] Colli Franzone P, Pavarino L, Scacchi S, Taccardi B. Performance evaluation of cardiac repolarization markers derived from unipolar electrograms and monophasic action potential: a simulation study. In 35th Computers in Cardiology Conference (CINC 2008). IEEE Proceedings, 2008; 593–596.

[2] Wyatt R. Comparison of estimates of activation and recovery times from bipolar and unipolar electrograms to in vivo transmembrane action potential durations. In Proc. IEEE/Eng. Med. Biol. Soc. 1980; 22–25.

[3] Haws C, Lux R. Correlation between in vivo transmembrane action potential durations and activation– recovery intervals from electrograms. Circulation 1990;81:281–288.

[4] Colli Franzone P, Pavarino L, Scacchi S, Taccardi B. Determining recovery times from transmembrane action potentials and unipolar electrograms in normal heart tissue. In Sachse F, Seemann G (eds.), FIMH07, volume 4466 of LNCS. Springer, 2007; 139–149.

[5] Franz M. Monophasic Action Potentials: Bridging Cells to Bedside. Futura Publishing Company, 2000.

[6] Nesterenko V, Weissenburger J, Antzelevitch C. Hybrid action potential etiology. cellular basis and method for recording the monophasic action potential. J Cardiovasc Eletrophysiol 2000;11:948–951.

[7] Colli Franzone P, Pavarino L, Scacchi S, Taccardi B. Monophasic action potentials generated by bidomain modeling as a tool for detecting cardiac repolarization times. Am J Physiol Heart Circ Physiol 2007;293:H2771–H2785.

[8] Henriquez C. Simulating the electrical behavior of cardiac tissue using the bidomain model. Crit Rev Biomed Eng 1993;21:1–77.

[9] Luo C, Rudy Y. A model of the ventricular cardiac action potential: depolarization, repolarization, and their interaction. Circ Res 1991;68(6):1501–1526.

[10] Colli Franzone P, Pavarino L, Scacchi S. Dynamical effects of myocardial ischemia in anisotropic cardiac models in three dimensions. Math Mod Meth Appl Sci 2007; 17(12):1965–2008.

[11] Colli Franzone P, Pavarino L. A parallel solver for reaction-diffusion systems in computational electrocardiology. Math Mod Meth Appl Sci 2004;14(6):883–911.

[12] Balay S, Buschelman K, Gropp D, Kaushik D, Knepley M, Curfman McInnes L, Smith B, Zhang H. PETSc Web page, 2001. Http://www.mcs.anl.gov/petsc.

[13] Scacchi S, Colli Franzone P, Pavarino L, Taccardi B. A reliability analysis of cardiac repolarization time markers. Math Biosci 2009;219:113–128.

[14] Scacchi S, Colli Franzone P, Pavarino L, Taccardi B. Computing cardiac recovery maps from electrograms and monophasic action potentials under heterogeneous and ischemic conditions. Math Mod Meth Appl Sci 2010; 20(7):1089–1127.



Address for correspondence:

Luca F. Pavarino

Dept. of Mathematics/ Università di Milano

Via Saldini 50, 20133 Milano, Italy

luca.pavarino@unimi.it